Z. Kristallogr. **2013**, *228*, 532–543 / **DOI** 10.1524/zkri.2013.1640

Structural properties of mullite-type $Pb(Al_{1-x}Mn_x)BO_4$

Th. M. Gesing*, [I], C. B. Mendive[II], M. Curti[II], D. Hansmann[III], G. Nénert[IV], P. E. Kalita[V], K. E. Lipinska[VI], A. Huq[VII], A. L. Cornelius[V] and M. M. Murshed[I]

[I] Chemische Kristallographie fester Stoffe, Institut für Anorganische Chemie, Universität Bremen, Leobener Straße/NW2, 28359 Bremen, Germany
[II] Departamento de Química, Facultad de Ciencias Exactas y Naturales, Universidad Nacional de Mar del Plata, Dean Funes 3350, B7600AYL, Mar del Plata, Argentina
[III] Departamento de Física, Facultad de Ciencias Exactas y Naturales, Universidad Nacional de Mar del Plata, Dean Funes 3350, B7600AYL, Mar del Plata, Argentina
[IV] Institut Laue-Langevin, 6 Rue Jules Horowitz, 38042 Grenoble Cedex 9, France
[V] Department of Physics and Astronomy, University of Nevada Las Vegas, Box 4002, Las Vegas, NV, 89154-4002, USA
[VI] Department of Mechanical Engineering, University of Nevada Las Vegas, 4505 Maryland Parkway, Box 454009, Las Vegas, NV 89154-4009, USA
[VII] Chemical and Engineering Materials Division, Oak Ridge National Laboratory, Oak Ridge, TN 37831-6475, USA

Received April 5, 2013; accepted May 22, 2013
Published online: August 12, 2013

Mullite-type / Crystal structure / Thermal expansion / Spectroscopy / Density functional theory

Abstract. We report on the structural characterization of the mullite-type $PbAl_{1-x}Mn_xBO_4$ series using neutron, synchrotron and in-house X-ray powder diffraction, Raman spectroscopy and density functional theory (DFT) calculations. The planar geometry of the BO_3 group changes only slightly over the whole composition range. The rigid BO_3 group plays the dominant roles in the thermal contraction in the *a*-direction followed by expansion in the *b*- and *c*-directions, leading to a correlation $a \cdot b/c \sim$ unity. The unit-cell volume at zero-pressure and 0 K was obtained, as well evaluated as the isothermal bulk-modulus from pressure dependent synchrotron X-ray diffraction using a diamond anvil cell as well as DFT calculations. Thermal expansion of the metric parameters was modeled using a first-order Grüneisen approximation for the zero-pressure equation of state. We used the double-Debye-double-Einstein-Anharmonicity model to calculate the temperature-dependent internal energy of the crystalline end members. The simulation helped to understand the anisotropic thermal expansion and together with the experimental and calculated bulk moduli to approximate the thermodynamic Grüneisen parameters.

Introduction

The characteristic building units of mullite-type compounds are the edge sharing MO_6 octahedra, forming single Zweier chains [1] running parallel to the crystallographic *c*-axis. A well-known compound of this structural family is the mineral minium Pb_3O_4 [2] which was used in anticorrosion paint for years. In this phase Pb^{4+} cations are found at the center position of the octahedral chains (Pb1, green in Fig. 1 left), while the Pb^{2+} cations interconnect these octahedral chains (Pb2 and Pb3, yellow in Fig. 1 left) and stabilize the structure using their stereochemically active $6\,s^2$ lone electron pair (LEP, E in formula). Garnier *et al.* [3] and Gavarri *et al.* [4] reported on the displacive phase transition from the low-temperature *Pbam* structure into the high-temperature $P4_2/mbc$ polymorph. In the low-temperature orthorhombic structure a negative thermal expansion of the *a* lattice parameter was found together with a positive thermal expansion in the *b* direction with increasing temperature towards the phase transition. Further heating above $T_C = 170$ K gives rise to a positive thermal expansion of the tetragonal *a* parameter [3, 4], which represents the former orthorhombic *a* and *b* direction. In the orthorhombic arrangement the Pb^{4+} cations could be replaced by Sn^{4+} [2], as well as cations having a lower valence, resulting in the same orthorhombic crystal structure which is, with this chemical composition, stable at room-temperature. If Pb^{4+} ions are replaced by M^{3+} ions, one of the Pb^{2+} cations must also be replaced by a trivalent cation for charge balance. Such a mutual combination is found in $PbMBO_4$ phases (M = Ga, Al, Cr, Mn, Fe) first reported by Park *et al.* [5–7]. Comparing these two struc-

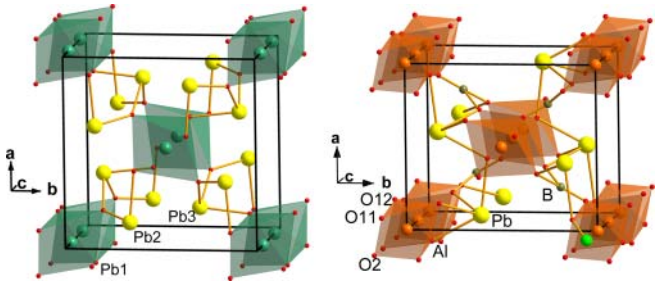

Fig. 1. Crystal structure of Pb_3O_4 (left) and $PbAlBO_4$ (right).

* Correspondence author (e-mail: gesing@uni-bremen.de)

ture types (Fig. 1), Pb1 in Pb_3O_4 is replaced for example by M, Pb2 remains as Pb and Pb3 is replaced by B. The resulting BO_3 group in the $PbMBO_4$ structure significantly increases the strength of the octahedral chains' interconnection, if one takes the average B−O bond length of 137.6(7) pm [6] into account with respect to the longer average Pb−O bond length of 237.6(7) pm [4]. In $PbMBO_4$ the $6s^2$ LEP of Pb^{2+} with a nido-like trigonal bipyramidal PbO_4E coordination is also stereochemically active [8], thus not influenced by the trigonal planar BO_3 group. Such a coordination of the LEP carrying cations is also found for the bismuth atoms in the $Bi_2M_4O_9$ mullite-types [9], however not in the closely related $Bi_2Mn_4O_{10}$ phases [10]. The strong influence of the BO_3 group on the properties of the $PbMBO_4$ phases is reported by Park *et al.* [6] as the driving force for the $\alpha \rightarrow \beta$ phase-transition of $PbAlBO_4$.

Additionally, the strong B−O bonds influence the thermal behavior of these compounds, resulting in a negative thermal expansion of the *a* lattice parameter, whereas a positive thermal expansion of the *b* and *c* lattice parameters is observed [4]. In this report, we use the non-standard *Pnam* setting with the octahedral chain parallel to the *c*-axis [11] instead of standard space group setting *Pnma* with the octahedral chains parallel to be *b* direction [5–7] for easy comparison of the crystal chemical properties with those of the other members of the mullite-type compounds. This report focuses primarily on: (i) a precise determination of the BO_3 group geometry using neutron powder diffraction data analysis, (ii) a complete description of the existing and observable infrared and Raman spectroscopy modes using experimental data and DFT calculations and (iii) the influence of the chemical substitution in the MO_6 building units on the anisotropic thermal expansion of the two end members of the $PbAl_{1-x}Mn_xBO_4$ solid solution. Both in-house X-ray and Raman spectroscopy served for the complementary results.

Experimental

Synthesis

Powder samples of the series $Pb(Al_{1-x}Mn_x)BO_4$ with $x = 0-1$ in successive steps of 0.1 were synthesized using the glycerine method [12]. For each compound a stoichiometric mixture of the metal-nitrates $Pb(NO_3)_2$, $Al(NO_3)_3 \cdot 9\,H_2O$ and $Mn(NO_3)_2 \cdot 4\,H_2O$ was heated together with boric acid, 50 mL deionized water and 10 wt% glycerine in a three step process at 353 K, 473 K and 973 K for 1 h, 2 h and 24 h, respectively. In the first heating step, in a glass beaker, the NO_x was released from the sample while stirring until a highly viscous mass was obtained. In the second step this mass was dried resulting in the formation of foam. After grinding, the amorphous powder was pressed into pellets and finally heated in a platinum crucible. To remove small impurities all samples were washed with diluted nitric acid after the final heat treatment [13]. The ^{11}B-enriched samples were produced using $H_3{}^{11}BO_3$ for neutron diffraction experiments to avoid neutron absorption of ^{10}B isotope.

X-ray and neutron diffraction

Temperature-dependent diffraction

All synthesized samples were investigated using X-ray diffraction measurements collected on a Panalytical MPD powder diffractometer in Bragg-Brentano geometry, equipped with a secondary Ni filter, CuK_α radiation and a X'Celerator multi-strip detector. The structural refinements were performed with the fundamental parameter approach using the "Diffrac^{Plus} Topas 4.2" (Bruker AXS GmbH, Karlsruhe) software. For the Rietveld refinements the starting atomic coordinates were taken from the room-temperature neutron diffraction data of $PbAlBO_4$ [6]. High-temperature data were collected on the same instrument with an attached Anton Paar HTK1200N heating chamber. Samples were prepared in a flat corundum sample holder using acetone to submerge the fine powder producing small evaporation channels which served for additional space for the thermal expansion of the compound. Measurements were carried out at 298 K and from 323 K to 1023 K with 50 K steps for $PbAlBO_4$, and up to 1123 K for $PbMnBO_4$. Each diffraction pattern was recorded from 10° to 120° 2θ with a step size of 0.0167° and a 50 s/step total data collection time. Temperature-dependent lattice parameters were calculated using Pawley fits [14] that insure the best description of the reflection profile enabling accurate lattice parameter determinations.

Room-temperature neutron diffraction data were collected on the D2B high-resolution powder diffractometer at the Institut Laue Langevin (Grenoble, France). Approx. 6 g of ^{11}B enriched $Pb(Al_{1-x}Mn_x)^{11}BO_4$ were loaded in a vanadium container of 11 mm diameter. The measurements were carried out at a wavelength corresponding to the (335) Bragg reflection of a germanium monochromator. The neutron detection was performed with ^3He counting tubes spaced at 1.25° intervals and a complete diffraction pattern was obtained after about 25 steps of 0.05° in 2θ. After the data collection, intensity data were extracted in two ways. First, only a narrow range in the middle of the 2D detector was used to obtain high-resolution data minimizing the curve of the Debye–Scherrer rings. Secondly, the whole detector range was evaluated resulting in lower resolution data with higher intensity. Both datasets were used for a combined refinement of the crystal structure; the high-resolution data increases the accuracy of the lattice parameters and the high-intensity data enhances the accuracy of the positional parameters. For the structure refinements three sets of powder diffraction data were used for the same sample: high intensity neutron data, high resolution neutron data and X-ray data. The lattice parameters obtained from the X-ray data were used to refine the neutron wavelength, which was calculated to be $1.59435(5) \cdot 10^{-10}$ m.

High-temperature neutron data were measured using a furnace, in which the sample was contained in a quartz tube in order to prevent any reaction of the sample with the heating elements. Despite the fact that the quartz tube creates additional and uneven background, the data at room-temperature used here were also collected within the quartz tube. Measurements above room-temperature were carried out between 370 K and 870 K in 100 K steps. Be-

fore each data collection the temperature was held for 15 minutes to equilibrate the sample. The collected data were evaluated as described above for high-intensity and high-resolution data. For the structure refinements only the two neutron diffraction data sets were used and the displacement parameters of lead and aluminum were as well restrained to each other as those of the three oxygen positions.

Low temperature neutron time of flight data were collected on Powgen high resolution diffractometer at Oak Ridge National Laboratory (Oak Ridge, Tennessee, USA). Approx. 5 g of ^{11}B enriched $PbAl^{11}BO_4$ was loaded in a vanadium container of 8 mm diameter. Temperature-dependent data were collected from 10 K to 90 K in 5 K steps followed by 10 K steps up to 300 K using a close cycle refrigeration system. Longer datasets (1.5 hours) were collected at 10, 100, 200 and 300 K which covered a *d*-spacing range from $0.3 \cdot 10^{-10}$ m to $6.2 \cdot 10^{-10}$ m, while the rest of the data were collected for 15 minutes spanning a *d* range of $0.4 \cdot 10^{-10}$ m to $3.6 \cdot 10^{-10}$ m.

Pressure-dependent diffraction

High-pressure, in situ, angle dispersive, synchrotron X-ray diffraction measurements were performed at the 16-IDB beamline of the High Pressure Collaborative Access Team, Advanced Photon Source, Argonne National Laboratory, USA. The sample-detector distance and geometric parameters were calibrated using a CeO_2 standard reference material from the National Institute of Standards and Technology. The sample of fine powder of $PbAlBO_4$ was compressed, at ambient temperature, in a symmetric type diamond anvil cell, using diamonds of 300 μm culets. A rhenium gasket was pre-indented to a thickness of ~50 μm. The sample chamber consisted of a 120 μm diameter hole, drilled in the pre-indented rhenium gasket. For pressure readings during compression, fragments of gold foil were mixed-in with the samples and used to measure pressure using the equation of state of gold by Anderson *et al.* [15]. To insure quasi-hydrostatic pressure conditions, compression was carried out with Ne as a quasi-hydrostatic pressure transmitting medium, which was loaded into the sample chamber at about $1.38 \cdot 10^8$ Pa (20,000 psi), using the gas loading setup of Sector 13 of APS, ANL [16]. Diffraction pattern were collected from ambient pressure up to 10.9 GPa in several pressure steps.

Based on Rietveld structure refinements using X-ray diffraction pattern we analyzed the pressure evolution of the unit cell volume of $PbAlBO_4$. Pressure-volume data collected up to 10.9 GPa were fitted with the 3rd order Birch–Murnaghan [17, 18] equation of state (EoS):

$$P(V) = \frac{3}{2} K_0 \left[\left(\frac{V_0}{V}\right)^{7/3} - \left(\frac{V_0}{V}\right)^{5/3} \right] \times \left\{ 1 + \frac{3}{4} (K_0' - 4) \left[\left(\frac{V_0}{V}\right)^{2/3} - 1 \right] \right\}, \quad (1a)$$

where V_0 and V are the unit cell volume at ambient pressure and unit cell volume at a given pressure, respectively, K_0 is the bulk modulus at ambient pressure and K_0' its pressure derivative. The EoS fit yielded the following experimental values of bulk modulus and its pressure derivative for $PbAlBO_4$: $K_0 = 76.1(6)$ GPa, $K_0' = 8.3(13)$ with $V_0 = 321.93(1) \cdot 10^{-30}$ m^3.

Spectroscopy

The room-temperature Raman spectra were collected using pressed powder of the respective samples. The spectra were recorded on a LabRam ARAMIS (Horiba Jobin Yvon) Micro-Raman spectrometer equipped with a laser working at 633 nm and less than 20 mW. The use of a 50× long working distance objective (Olympus) with a numerical aperture of 0.55 provides a focus spot of about 2 μm diameter when closing the confocal hole to 200 μm. Raman spectra were collected in the range 50 cm^{-1} to 1500 cm^{-1} with a spectral resolution of approximately 2 cm^{-1} using a grating of 1800 grooves/mm and a thermoelectrically-cooled CCD detector (Synapse, 1024×256 pixels). The spectral positions were calibrated against the Raman mode of Si before and after the sample measurements. The position of the Si peak was repeatedly measured against the Rayleigh line (0.0 cm^{-1}) yielding a value of 520.7 ± 0.1 cm^{-1}. The linearity of the spectrometer was calibrated against the emission lines of a neon lamp. For comparison, the infrared data collected with the KBr method were taken from [13]. The low-temperature Raman data at 78(1) K were collected on pressed sample using a Linkam cooling stage (THMS600) attached to a pump (LNP95 Cooling Pump) that provides a continuous flow of liquid nitrogen.

DFT calculations

Periodic calculations were performed with the crystalline orbital program CRYSTAL09 [19, 20], employing the PW1PW hybrid Hartree Fock – Density Functional Theory (HF-DFT) method [21]. All structures were optimized starting from the experimental crystallographic data. The basis sets were taken from the CRYSTAL website database [22]. The Monkhorst-Pack shrinking factor was set to 4 after checking energy convergence of the structures, that is, 27 independent *k*-points in the irreducible Brillouin zone were taken. A high spin ferromagnetic configuration was used for manganese in $PbMnBO_4$.

Bulk modulus

Geometry optimizations were done under a hydrostatic constant pressure as implemented in CRYSTAL09 [19, 20]. By changing the pressure to the desired value, the different pressure-dependent unit-cell volumina were obtained. The constant pressure constrained geometry optimizations were performed at 0, 5, 10, 15, 20 and 30 GPa for the aluminum compound, and at 0, 2, 4, 5, 6 and 7 GPa for the manganese compound (Fig. 2)

The given 3rd-oder Birch-Murnaghan isothermal EoS (Eq. (1a)) was used to calculate the bulk modulus $K_0 = 77.4(2)$ GPa and 52.7(18) GPa and the first derivative of the bulk modulus $K_0' = 6.5(19)$ and 8.4(36) using

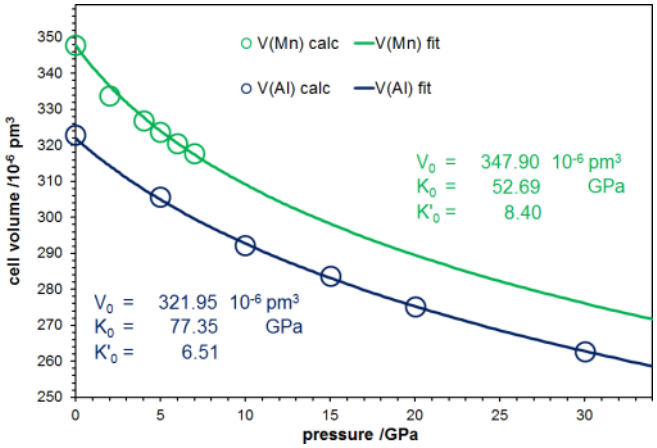

Fig. 2. DFT calculated pressure dependent volume change of $PbAlBO_4$ and $PbMnBO_4$ together with the 3rd-order Birch-Murnaghan EoS fit. Individual errors are within the symbols.

a zero-pressure volume $V_0 = 231.95(1) \cdot 10^{-30}\,\mathrm{m}^3$ and $347.9(1) \cdot 10^{-30}\,\mathrm{m}^3$ for $PbAlBO_4$ and $PbMnBO_4$, respectively. The pressure dependent DFT calculated unit-cell volume and the respective fits are plotted in Fig. 2.

Additionally, by varying the lattice parameter (as implemented in CRYSTAL09) and fitting the energy form of Eq. (1b) which is found by integration of the pressure,

$$E(V) = E_0 + \frac{9V_0K_0}{16}\left\{\left[\left(\frac{V_0}{V}\right)^{2/3} - 1\right]^3 K_0' + \left[\left(\frac{V_0}{V}\right)^{2/3} - 1\right]^2\left[6 - 4\left(\frac{V_0}{V}\right)^{2/3}\right]\right\} \quad (1b)$$

the same parameters, K_0, K_0' and V_0, were thus evaluated yielding 77.6(3) GPa, 6.9(21) and $322.10(1) \cdot 10^{-30}\,\mathrm{m}^3$ for the aluminum compound and 46.9(14) GPa, 8.4(23), and $347.9(1) \cdot 10^{-30}\,\mathrm{m}^3$ for the manganese compound. The results obtained by both different methods, *i.e.*, fitting Eqs. (1a) or (1b), are in good agreement. Nevertheless, one should be careful because of the different zero pressure volume calculated for $PbMnBO_4$. The deviation might be due to magneto-volume effect below 31 K described by Park *et al.* [7] because high-spin manganese was used for the 0 K DFT calculations.

IR and Raman modes

Harmonic frequencies and the intensities of the infrared modes at the Γ point of the Brillouin zone at 0 K were calculated by computing numerically the second derivatives of the energy with respect to the atomic positions, and diagonalizing the mass-weighted Hessian matrix in Cartesian coordinates, as implemented in CRYSTAL09 [23, 24]. The infrared (Table 1) and Raman (Table 2) modes were given as an output of the calculations (see column "Mode") and doubly verified by (a) visual inspection of every mode by means of a graphical interface program that displayed the atom movements, and (b) changing selected atomic masses to cause the shift of the corresponding mode (see column "Mode description").

Thermal expansion

The thermal expansion behavior has been described with respect to the internal energies following Senyshyn *et al.* [25]. We use an extended expression for the metric parameter M that represents either the cell volume V as physical meaningful description or the lattice parameters a, b or c for a comparable data evaluation:

$$M(T) = M_0 + k_{D1}U_{D1}(T) + k_{D2}U_{D2}(T) + k_{E1}U_{E1}(T) + k_{E2}U_{E2}(T) + k_AU_A(T) \quad (2)$$

k_{Di}, k_{Ei} and k_A are adjustable fitting parameters, describing the bulk modulus divided by the thermodynamic Grüneisen parameter, contributing to Debye quasi-harmonic (U_{Di}), Einstein harmonic (U_{Ei}) and anharmonic (U_A) internal energies, respectively:

$$U_{Di}(T) = \left[9\,N\,k_\mathrm{B}T\left(\frac{T}{\theta_{Di}}\right)^3 \int_0^{\theta_{Di}/T} \frac{x^3}{\mathrm{e}^x - 1}\,\mathrm{d}x\right], \quad (3)$$

$$U_{Ei}(T) = \left[\frac{3\,N\,k_\mathrm{B}\theta_{Ei}}{\mathrm{e}^{(\theta_{Ei}/T)} - 1}\right], \quad (4)$$

$$U_A(T) = \left[a_A\frac{3\,N\,k_\mathrm{B}\theta_A^2}{24\,T}\left[T\,\mathrm{e}^{(3\theta_A/T)} + 9\,T\,\mathrm{e}^{(2\theta_A/T)} - 12\,\theta_A\,\mathrm{e}^{(2\theta_A/T)} - 9\,T\,\mathrm{e}^{(\theta_A/T)} - 12\,\theta_A\,\mathrm{e}^{(\theta_A/T)} - T\right]\left[(\mathrm{e}^{(\theta_A/T)} - 1)^3\right]^{-1}\right], \quad (5)$$

where N refers to the number of atoms per unit cell ($PbMBO_4$: $N = 28$), k_B is the Boltzmann constant, θ_{Di} and θ_{Ei} are the characteristic Debye ($\theta_D = hc\omega_D/k_\mathrm{B}\mathrm{T}$) and Einstein ($\theta_E = hc\omega_\mathrm{E}/k_\mathrm{B}\mathrm{T}$) temperatures. a_A is the anharmonic parameter ($a_A = 1.0 \cdot 10^{-5}\,\mathrm{K}^{-1}$ – a reasonable approximate value is fixed for all the models in this report) and $\theta_A = \theta_{D1}$ for a single Debye oscillator, or weighted average of two Debye oscillators ($\theta_A = (|k_{D1}| \cdot \theta_{D1} + |k_{D2}| \cdot \theta_{D2})/(|k_{D1}| + |k_{D2}|)$) [9] where necessary. The total internal energy as the sum of the single contributions is given as Energy/unit cell. For the calculation of the molar internal energy the number of atoms per unit cell N is divided by the number of atoms per formula unit (Z) and multiplied with the Avogadro constant $N_A = 6.023 \cdot 10^{23}$ atoms/mole ($N/Z \cdot N_A$). This provides the internal energy in kJ/mole, as given in Fig. 3, for the respective formula unit which is in this case $PbMBO_4$. For the calculations reported here low-temperature data are available for $PbAlBO_4$. For $PbMnBO_4$ only data from room-temperature upwards could be measured which makes it in this case unnecessary to use two Debye contributions, used to describe a complicated low-temperature behavior. Nevertheless, a single Debye contribution could be calculated from the high-temperature contributions, at least with respect to the anharmonicity parameter. Additionally the thermal expansion coefficient (TEC), expressed as $\alpha_M = \Delta M/M \cdot 1/\Delta T$ ($M = V$, a, b, c) was calculated from the observed metric data and used as second fitting values to stabilize the calculations. In this way one can evaluate whether a linear

Table 1. Calculated infrared mode positions and intensities of $PbAlBO_4$ and $PbMnBO_4$ at 0 K.

$PbAlBO_4$				$PbMnBO_4$			
Wavenumber cm^{-1}	mode	Mode description[a]	Intensity %	Wavenumber cm^{-1}	mode	Mode description[a]	Intensity %
86.32	B_{2u}	Pb−O str	1.79	72.79	B_{2u}	Pb−O str	1.15
90.84	B_{1u}	Pb−O str	0.40	83.64	B_{1u}	Pb−O str	0.26
110.21	B_{3u}	O−Pb−O wa	1.09	84.09	B_{3u}	O−Pb−O wa	1.96
117.07	B_{2u}	Pb−O str	7.90	96.29	B_{2u}	Pb−O str	7.02
178.80	B_{1u}	O−M−O sci	2.87	127.56	B_{1u}	O−M−O sci	1.59
203.97	B_{1u}	O−Pb−O sci	2.66	159.21	B_{1u}	Pb−O str	3.72
216.98	B_{3u}	O−M−O sci	3.62	172.42	B_{3u}	O−M−O sci	2.77
262.47	B_{3u}	O−M−O sci	11.46	190.92	B_{3u}	O−M−O sci	4.20
266.74	B_{2u}	O−M−O sci	0.27	215.99	B_{2u}	O−M−O sci	0.69
317.46	B_{1u}	M−O−M wa	0.37	235.79	B_{1u}	O−M−O sci	0.88
321.17	B_{2u}	M−O−M wa	0.17	245.23	B_{2u}	M−O str	4.55
345.16	B_{3u}	O−B−O sci O−M−O sci	8.81	253.17	B_{3u}	O−M−O sci	1.49
374.51	B_{2u}	O−M−O sci O−B−O sci	6.51	287.08	B_{2u}	M−O−M wa	0.09
390.36	B_{3u}	O−M−O sci	9.67	307.42	B_{1u}	O−M−O sci	2.90
401.08	B_{1u}	O−M−O sci	5.03	327.36	B_{3u}	O−M−O sci	16.03
437.79	B_{2u}	M−O str	31.05	345.18	B_{2u}	M−O str	6.36
440.30	B_{3u}	M−O str O−M−O sci	3.84	362.41	B_{1u}	O−M−O sci + O−B−O sci	3.45
452.61	B_{1u}	O−M−O sci O−B−O sci	40.36	367.84	B_{3u}	O−M−O sci	1.53
496.13	B_{1u}	M−O str O−M−O sci	0.01	394.93	B_{1u}	M−O str	12.11
501.11	B_{2u}	O−M−O sci	11.47	403.70	B_{2u}	O−M−O sci	0.20
524.64	B_{2u}	O−M−O sci	0.95	430.64	B_{2u}	O−M−O sci	16.83
557.21	B_{1u}	O−M−O sci	8.17	474.34	B_{1u}	O−M−O sci	14.29
654.98	B_{1u}	O−B−O sci	0.89	589.43	B_{3u}	M−O str	38.10
664.76	B_{2u}	O−B−O sci	5.68	589.60	B_{1u}	M−O str	15.46
677.78	B_{3u}	O−B−O sci	8.97	600.24	B_{2u}	O−B−O sci	6.34
688.04	B_{1u}	O−M−O sci O−B−O wa	9.39	618.63	B_{1u}	O−B−O sci	3.69
690.27	B_{3u}	O−B−O sci	14.53	658.90	B_{2u}	O−B−O sci	1.63
706.75	B_{2u}	O−B−O wa	1.62	662.69	B_{3u}	O−B−O sci	0.90
721.35	B_{1u}	O−B−O wa	8.50	694.87	B_{2u}	O−B−O wa	7.02
733.55	B_{2u}	O−B−O sci	8.23	725.08	B_{1u}	O−B−O wa	2.94
969.12	B_{2u}	B−O str (s)	0.01	948.33	B_{2u}	B−O str(sy)	0.83
979.02	B_{1u}	B−O str (s)	<0.01	949.22	B_{1u}	B−O str(sy)	2.13
1267.62	B_{3u}	B−O str (as)	100.00	1181.13	B_{3u}	B−O str(as)	100.00
1305.93	B_{2u}	B−O str (as)	24.15	1311.95	B_{2u}	B−O str(as)	24.44
1310.68	B_{1u}	B−O str (as)	36.04	1312.87	B_{1u}	B−O str(as)	60.65

a: str: streching, wa: wagging, sci: scissoring, tw: twisting, ro: rocking, s: symmetric, as: asymmetric

thermal expansion coefficient could be observed (which could easily be identified in a constant TEC *vs.* temperature behavior) and if so, in which temperature range.

The limited number of the measured data, which is true for the data set of the aluminum compound and even more for the manganese containing phase, makes the volume modeling via regression analysis using Eq. (2) quite unstable. This means that, especially for $PbMnBO_4$, as a consequence of the missing information in the low-temperature regime, the chance that the regression converges in a local minimum and yields wrong results increases. Taking this into account, the influence of different initial values on the results of the regression was systematically tested to assure the quality of the calculated parameters. The median values have been calculated from 1000 single fits. For each of these fits the experimental data were slightly modified via a random generator within their estimated standard deviations. The computation time of these extensive calculations was minimized using a relatively fast quasi-Newton method for the fitting. The given regression results (Table 3) are obtained using initial values, which correspond to the areas (bins) of the highest conversion probability. The confidence intervals of the results were calculated using the Monte Carlo technique and are based on the experimental errors for determination of the lattice parameters.

The unit cell internal energy of the thermal lattice vibrations $U(T)$ could be used in the 1st-order Grüneisen

Table 2. Calculated 0 K and experimental 78 K and 298 K Raman mode positions of $PbAlBO_4$ and $PbMnBO_4$.

$PbAlBO_4$					$PbMnBO_4$				
Wavenumber/cm^{-1}			mode	Mode description[a]	Wavenumber/cm^{-1}			mode	Mode description[a]
0 K DFT	78 K exp	298 K exp			0 K DFT	78 K exp	298 K exp		
59.54			A_g	Pb−O str	52.05			A_g	Pb−O str
77.42			B_{1g}	O−Pb−O wag	63.57			B_{2g}	Pb−O−Pb rock
79.32	81.4	80.5	B_{2g}	O−Pb−O wag	65.42			B_{1g}	O−Pb−O wag
101.31			A_g	Pb−O str	91.38			B_{3g}	Pb−O str
104.33	106.8	106.2	B_{3g}	Pb−O str	96.42	104.2	103.7	A_g	Pb−O str
119.65			B_{3g}	Pb−O str	106.93	108.6	107.4	B_{3g}	Pb−O str
180.79	177.2	174.1	A_g	O−Pb−O sci	159.98	141.1	132.9	A_g	O−Pb−O sci
217.88	214.1	211.4	B_{3g}	Pb−O str	187.69	186.7	184.1	B_{2g}	Pb−O−Mn wag
234.86	231.5	229.6	B_{2g}	Pb−O−Al wag	189.54			B_{3g}	Pb−O str
236.69			B_{1g}	Pb−O−Al wag	198.24	197.4	207.4	B_{1g}	O−Pb−O rock
302.29	300.1	298.8	B_{2g}	O−Pb−O twist	213.92	217.7	208.7	A_g	Mn−O str
314.07			B_{1g}	Pb−O str	226.75			B_{2g}	Pb−O−Mn wag
315.72	316.7	–	B_{3g}	Al−O−Al wag	251.35	245.2	242.3	B_{3g}	O−Mn−O twist
334.66	329.9	324.5	A_g	Al−O str	273.26	265.8	263.2	B_{1g}	O−Mn−O wag
349.81	351.4	349.7	A_g	Al−O−Al twist	283.15	284.4	283.0	A_g	Mn−O−Mn wag
366.19	371.5	368.2	B_{2g}	O−Al−O twist	294.72	295.4	291.2	B_{2g}	O−Mn−O rock
375.09	373.3	369.7	B_{3g}	Al−O str	360.00	354.3	352.0	A_g	Mn−O−Mn wag
409.74	411.9	408.5	B_{1g}	Al−O str	360.87			B_{3g}	Mn−O str
415.57	423.9	423.3	A_g	O−Al−O twist + O−B−O sci	363.82	364.8	365.1	B_{1g}	Mn−O str
475.97			B_{3g}	Al−O−Al wag + O−B−O sci	426.66			B_{3g}	O−Mn−O twist
536.09	534.0	532.2	A_g	O−B−O sci	524.86	515.9	512.9	A_g	O−B−O sci
540.83			B_{2g}	O−B−O sci	543.05	531.0	527.5	B_{3g}	Mn−O−Mn wag
575.76			B_{3g}	B−O str	561.60			B_{2g}	O−B−O sci
608.61			B_{1g}	O−Al−O twist	599.28	588.9	589.2	B_{1g}	O−B−O sci
651.34			B_{1g}	O−B−O sci	622.02	616.0	614.4	B_{3g}	O−B−O sci
665.42			B_{3g}	O−B−O sci	633.04			A_g	O−B−O sci
669.50	669.1	667.9	A_g	O−B−O sci	633.56	626.7	625.8	B_{1g}	O−B−O sci
708.93			A_g	O−B−O wag	685.13			B_{2g}	O−B−O sci
712.33	713.8	713.4	B_{2g}	O−B−O sci	694.99	–	690.5	A_g	O−B−O wag
738.41	744.8	744.5	B_{3g}	O−B−O wag	732.00			B_{3g}	O−B−O wag
958.48			B_{3g}	B−O str (s)	934.04	918.0	916.8	B_{3g}	B−O str (s)
975.06	967.6	966.9	A_g	B−O str (s)	947.36	929.9	927.6	A_g	B−O str (s)
1261.78	1225.7	1223.8	B_{2g}	B−O str (as)	1181.33	1139.9	1139.7	B_{1g}	B−O str (as)
1264.22			B_{1g}	B−O str (as)	1183.26			B_{2g}	B−O str (as)
1265.86	1230.6	1228.9	A_g	B−O str (as)	1280.89	1224.0	1219.1	A_g	B−O str (as)
1367.43	1325.0	1322.9	B_{3g}	B−O str (as)	1371.31	1303.1	1297.9	B_{3g}	B−O str (as)

a: str: stretching, wag: wagging, sci: scissoring, twist: twisting, rock: rocking, s: symmetric, as: asymmetric

approximation to the zero-pressure EoS [26] (Eq. 6) with V_0 as zero-pressure volume at 0 K to calculated $Q = K_T/\gamma$.

$$V(T) = V_0 + \frac{U(T)}{Q}\,. \tag{6}$$

With K_T equivalent to the Birch-Murnaghan bulk-modulus K_0 the thermodynamic Grüneisen-parameter γ can be derived.

Results and discussion

The success of the aluminum replacement by manganese can be seen in the systematic change of the lattice parameters as well as the cell volume as given in Fig. 4. The use of ^{11}B for the synthesis of the $Pb(Al_{1-x}Mn_x)^{11}BO_4$ compounds did not affect the metric parameters. They do not deviate significantly from the reported metric parameters [13] calculated from the in-house X-ray diffraction data. The anisotropy parameter (Eq. (7)) increases with increasing manganese content in the $PbMBO_4$ phase.

$$A = |a - b| + |a - c| + |b - c|\,. \tag{7}$$

This clearly shows that the incorporation of bigger manganese ($r(^{VI}Mn^{3+(LS)}) = 72$ pm and $r(^{VI}Al^{3+}) = 67.5$ pm [27]) anisotropically influences the expansion of the lattice parameters. Interestingly, the evolution of the a and b lattice parameters with respect to the c parameter expressed as $a \cdot b/c$ (normalized with respect to the value of the pure aluminum content compound, Fig. 4) shows that the substitution has only a small effect on the directions perpendicular (a, b) and parallel (c) to the octahedral chains. This finding supports the common structural features as being the characteristic building units of mullite-type compounds.

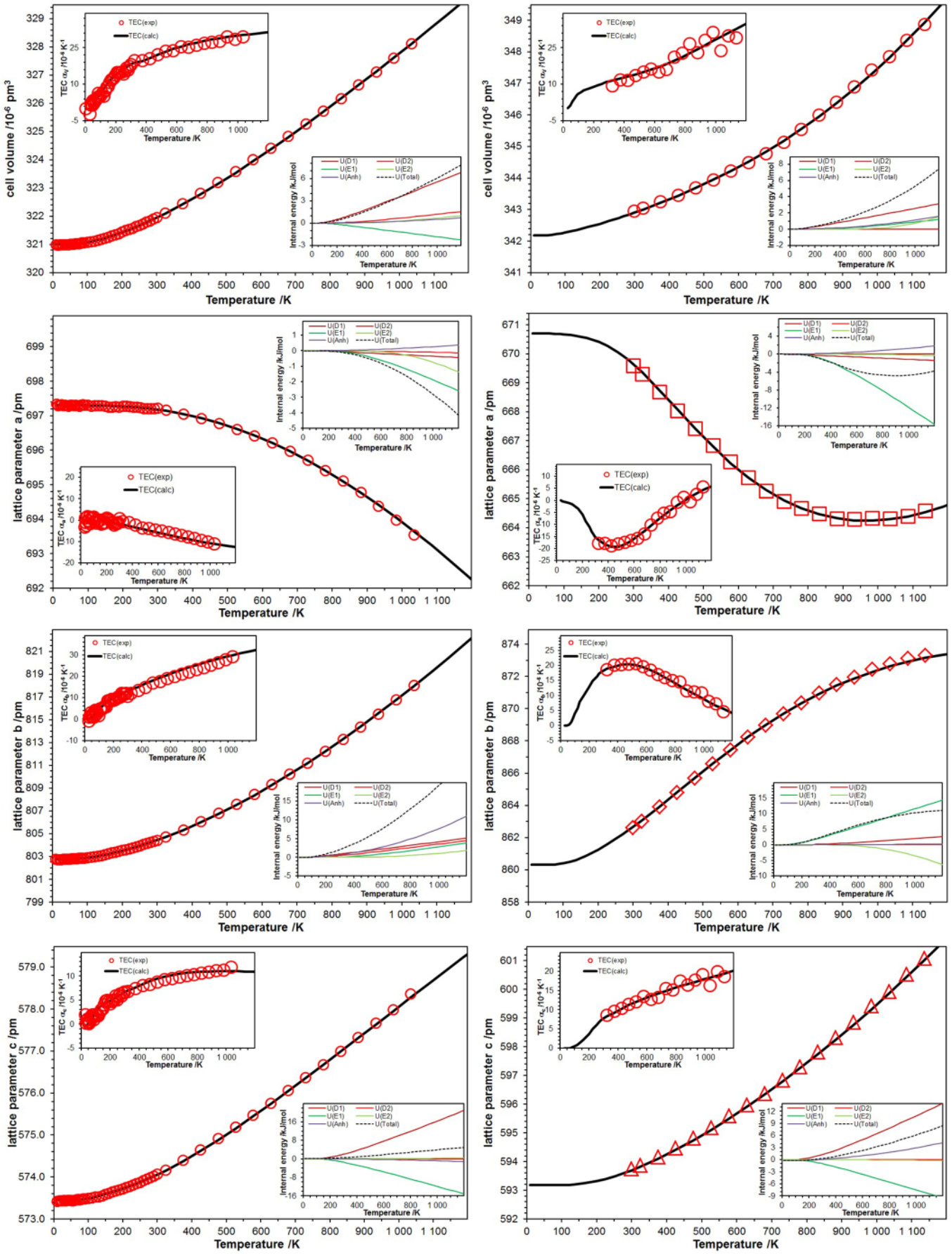

Fig. 3. Experimental thermal behavior and calculated model curves of the metric parameters (red symbols experimental, black symbols and line modeled data) of $PbAlBO_4$ (left) and $PbMnBO_4$ (right). The left inserts show the thermal expansion coefficient (TEC), the right inserts the internal energy calculated for the respective Debye ($U(Di)$), Einstein ($U(Ei)$) and anharmonicity (U(Anh)) contributions to the total energy (U(Total)).

Table 3. Median values and the 95% C.I. resulting from the fitting of the temperature-dependent metric parameters of $PbAlBO_4$ and $PbMnBO_4$.

Metric parameter	V(Al)/V(Mn)	a(Al)/a(Mn)	b(Al)/b(Mn)	c(Al)/c(Mn)
Model[a]	DDEEA/DEEA	DDEEA/DEEA	DDEEA/DEEA	DDEEA/DEEA
0 K[b]	$321.0^{+0.1}_{-0.1}$ $/342.2^{+0.1}_{-0.1}$	$697.3^{+0.1}_{-0.1}$ $/670.7^{+0.1}_{-0.2}$	$802.8^{+0.1}_{-0.1}$ $/860.4^{+0.1}_{-0.1}$	$573.4^{+0.1}_{-0.1}$ $/593.4^{+0.2}_{-0.3}$
$k_{D1}/10^{-12}$	$8.21^{+1.8}_{-4.5}$ $/2.90^{+0.21}_{-0.54}$	$-0.23^{+0.19}_{-0.15}$ $/-1.28^{+1.09}_{-0.32}$	$3.23^{+1.2}_{-0.4}$ $/3.77^{+0.24}_{-0.52}$	$8.41^{+4.8}_{-5.9}$ $/13.89^{+2.8}_{-1.0}$
θ_{D1}/K	430^{+120}_{-80} $/322^{+25}_{-5}$	517^{+33}_{-117} $/301^{+18}_{-33}$	200^{+126}_{-5} $/1506^{+29}_{-39}$	913^{+25}_{-100} $/981^{+65}_{-42}$
$k_{D2}/10^{-12}$	$3.0^{+2.1}_{-2.9}$ /–	$-3.7^{+1.6}_{-0.5}$ /–	$10.1^{+1.5}_{-2.4}$ /–	$9.5^{+6.8}_{-5.9}$ /–
θ_{D2}/K	1415^{+124}_{-109} /–	1933^{+48}_{-225} /–	1033^{+39}_{-52} /–	673^{+53}_{-60} /–
$k_{E1}/10^{-12}$	$-3.81^{+3.8}_{-3.1}$ $/1.90^{+0.44}_{-0.60}$	$-0.09^{+0.1}_{-2.2}$ $/-20.74^{+0.50}_{-1.49}$	$1.52^{+2.6}_{-1.5}$ $/14.55^{+0.87}_{-0.30}$	$-0.01^{+1.07}_{-0.01}$ $/-8.66^{+0.82}_{-2.19}$
θ_{E1}/K	294^{+56}_{-44} $/1363^{+7}_{-15}$	1659^{+68}_{-60} $/1021^{+20}_{-16}$	1366^{+39}_{-52} $/449^{+43}_{-27}$	563^{+350}_{-9} $/569^{+573}_{-46}$
$k_{E2}/10^{-12}$	$0.4^{+2.1}_{-0.4}$ $/14.22^{+0.96}_{-1.16}$	$-7.5^{+1.2}_{-2.5}$ $/34.87^{+0.79}_{-0.53}$	$12.3^{+2.4}_{-2.0}$ $/-29.85^{+0.62}_{-0.62}$	$-12.6^{+13.8}_{-7.4}$ $/-0.74^{+2.4}_{-0.8}$
θ_{E2}/K	2115^{+143}_{-156} $/4463^{+27}_{-6}$	3136^{+864}_{-98} $/2634^{+10}_{-10}$	2994^{+205}_{-74} $/3406^{+83}_{-62}$	539^{+167}_{-25} $/2653^{+580}_{-48}$
$k_A/10^{-12}$	-88.3^{+38}_{-62} $/-72^{+63}_{-99}$	$-0.1^{+0.1}_{-0.3}$ $/-78.3^{+0.8}_{-0.5}$	$-24.1^{+13.6}_{-5.8}$ $/-62^{+34}_{-52}$	2.3^{+13}_{-12} $/-499^{+53}_{-4}$
$a_A/10^{-5}\,K^{-1}$	1	1	1	1
θ_A/K	θ_{D1}	θ_{D1}	θ_{D1}	θ_{D1}

a: DDEEA = double Debye double Einstein Anharmonic model, DEEA = single Debye double Einstein Anharmonic model.
b: Cell parameters a, b, c and cell volume V at 0 K are given in pm and 10^6 pm^3, respectively. The value probabilities are given as super- and subscript numbers.

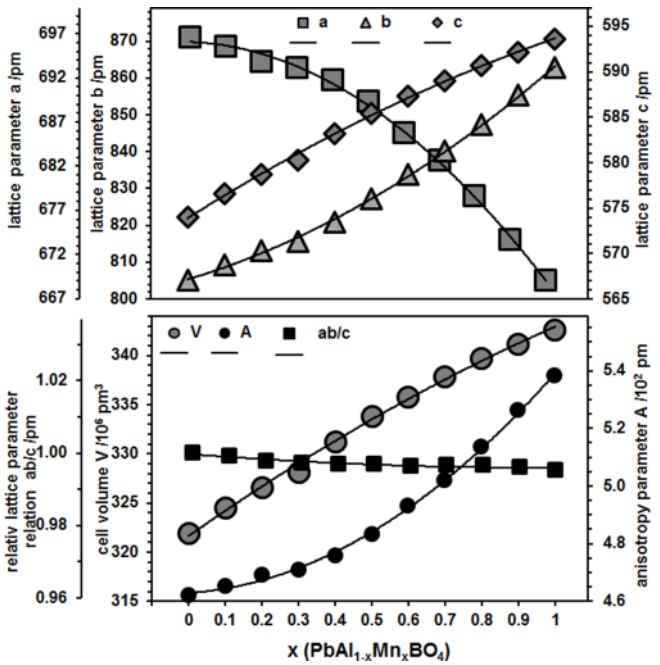

Fig. 4. Development of the metric parameters, the relative lattice parameter relations and the metric anisotropy parameter in $Pb(Al_{1-x}Mn_x)BO_4$ with respect to the chemical composition.

With respect to the strong changes of the lattice parameters, or the anisotropy parameter, the small deviation from a nearly constant $a \cdot b/c$ relation must be regarded as influenced by internal structural changes. An increasing distortion of the octahedra with increasing manganese content (Jahn–Teller distortion [28]) can be ruled out as reason for this observation, because of the almost zero-slope linearity of the $a \cdot b/c$ curve. The same is true for the eccentricity parameter [29] describing the influence of the 6 s^2 lone electron pair's stereo-chemical activity, which is linearly correlated to the average radius of the octahedral cations [13].

If neither the trivalent aluminum/manganese cations with MO_6 octahedra nor lead with PbO_4E nido-like trigonal bipyramidal coordination show any significant contribution to the structural changes, this behavior must be assigned, by default, to the trigonal coordinated boron cations. It has been reported [13] that the infrared active ν_1-mode of the BO_3 group at around 960 cm^{-1} for $PbAlBO_4$ is not visible, whereas the same mode was clearly seen at around 920 cm^{-1} in $PbMnBO_4$ (Fig. 5). From the DFT calculations of the infrared active mode intensities it can be seen indeed that the symmetric B–O stretching modes in $PbAlBO_4$ (at 969 cm^{-1} and 979 cm^{-1}

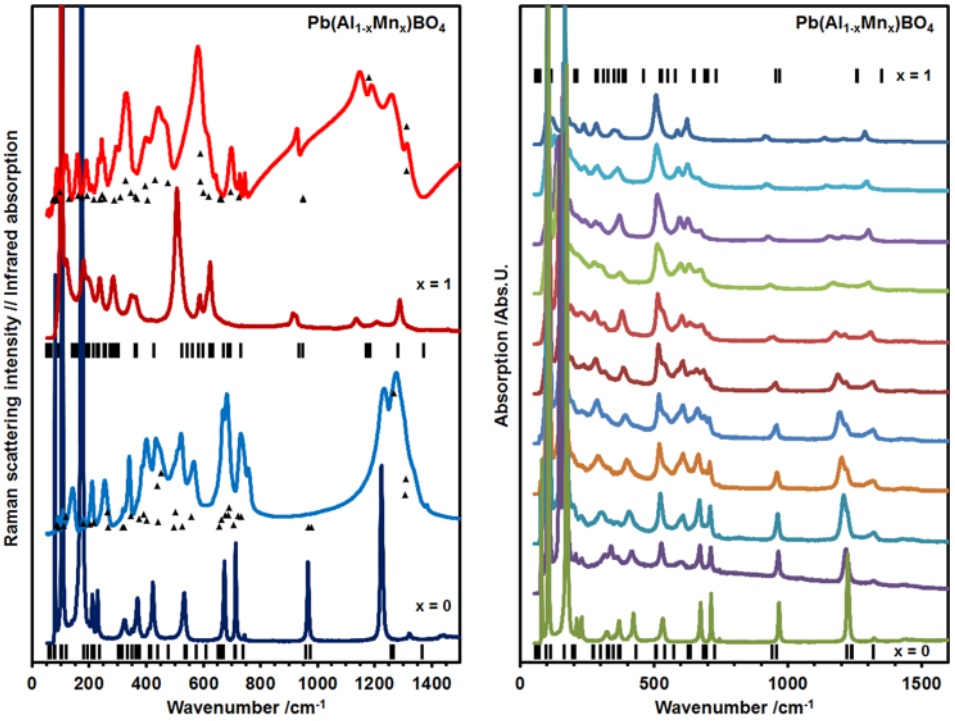

Fig. 5. Room-temperature Infrared (data taken from [13]) and Raman spectra (left) together with the calculated 0 K infrared mode frequencies and intensities (▲) and Raman 0 K mode frequencies (|) of $PbMBO_4$ (M = Al, Mn). The Raman spectra of $Pb(Al_{1-x}Mn_x)BO_4$ solid solution with respect to the chemical composition are given in the right part ($x = 0.1$ includes impurities).

at 0 K) show only negligible intensities, while the same modes in $PbMnBO_4$ (at 948 cm^{-1} and 949 cm^{-1} at 0 K, which could not be resolved during the measurements) show significant intensity contributions. This was explained with a highly symmetric BO_3-group (local D_{3h} symmetry) for the aluminum and a reduced symmetry (C_S) for the manganese compound. Nevertheless, the local D_{3h} symmetry for the aluminum compound could only be assumed within the resolution of the spectra but is disproved by the DFT calculations.

The Raman spectra of the $PbAl_{1-x}Mn_xBO_4$ solid solution series are shown in Fig. 5. On the basis of clearly discernible band maxima and shoulders, fitting of the scattering features required 23 and 22 fitted bands for $PbAlBO_4$ and $PbMnBO_4$ phase, respectively, in the range between 50 cm^{-1} and 1400 cm^{-1}. The primitive unit cell of $PbMBO_4$ contains 28 atoms with $Z = 4$, resulting in a total number of 84 vibrational modes. Factor group analysis predicts 36 Raman active, 38 infrared active and 10 acoustic modes for the selective site symmetries in space group *Pnam*. The technical limitation of the instrument and the low intensity of bands reduce the number of the observed modes from the theoretical ones (Table 2). The experimentally observed modes associated with the MO_6 and PbO_4 polyhedra conform closely to the corresponding predicted frequency values. However most of the BO_3 modes showed a reasonable deviation in frequency. In this regard, the theoretical calculations with the natural boron and the experimental observation on the ^{11}B-enriched samples must be considered. Although the average B−O bond distance slightly increases with a complete substitution of aluminum with manganese, the shift of the corresponding modes associated with the $PbAlBO_4$ and $PbMnBO_4$ is significant. For $PbAlBO_4$ a single pseudo-Voigt symmetric band profile at about 967(1) cm^{-1} was observed. This mode gradually broadens and can be resolved as a single mode till at $x = 0.4$. At $x = 0.5$ this mode requires two bands to be fitted well due to two noticeable maxima at 955(1) cm^{-1} and 943(1) cm^{-1}. With increasing manganese in the phase they both shift toward low frequency values, and the intensity of the lower-frequency mode successively increases and finally dominates over the higher-frequency counterpart when it reaches at 916(1) cm^{-1} for $x = 1$. The appearance and its intensity behavior may be related to the lowering of the local symmetry of the BO_3 since the deviation between two B−O distances (B−O2, B−O12) gradually increases with increasing manganese content (Fig. 6). Moreover, the planarity of BO_3 groups averaged from the diffraction data must be taken into account. In fact, a careful Rietveld refinement of the neutron powder diffraction data demonstrates that the boron atom is located as much as 0.8(1) pm above the BO_3-plane. This observation at least validates our early prediction based on the infrared spectra [13].

From the refinements of the neutron powder diffraction data the position of the boron and oxygen atoms can be refined much more accurately as compared to X-ray data. On the other hand parameters of heavy atoms like lead could be much better refined using X-ray diffraction. Therefore we used a combined refinement of neutron and X-ray powder diffraction data accepting the different displacement parameters obtained from neutron and X-ray data to be treated with only one displacement parameter each. From these refinements a continuous increase of the M−O11 and M−O12 distances, as given in Fig. 6, representing the equatorial plane of the MO_6 octahedron (Fig. 1) with increasing manganese content is observed. The corresponding M−O2 distances first decrease from 200.1(2) pm to 198.3(4) pm at about $x = 0.7$ and then remain around this value. The average M−O distance increases linearly up to 50 % substitution, and with a slightly higher slope with higher manganese content, indicating the dominance of

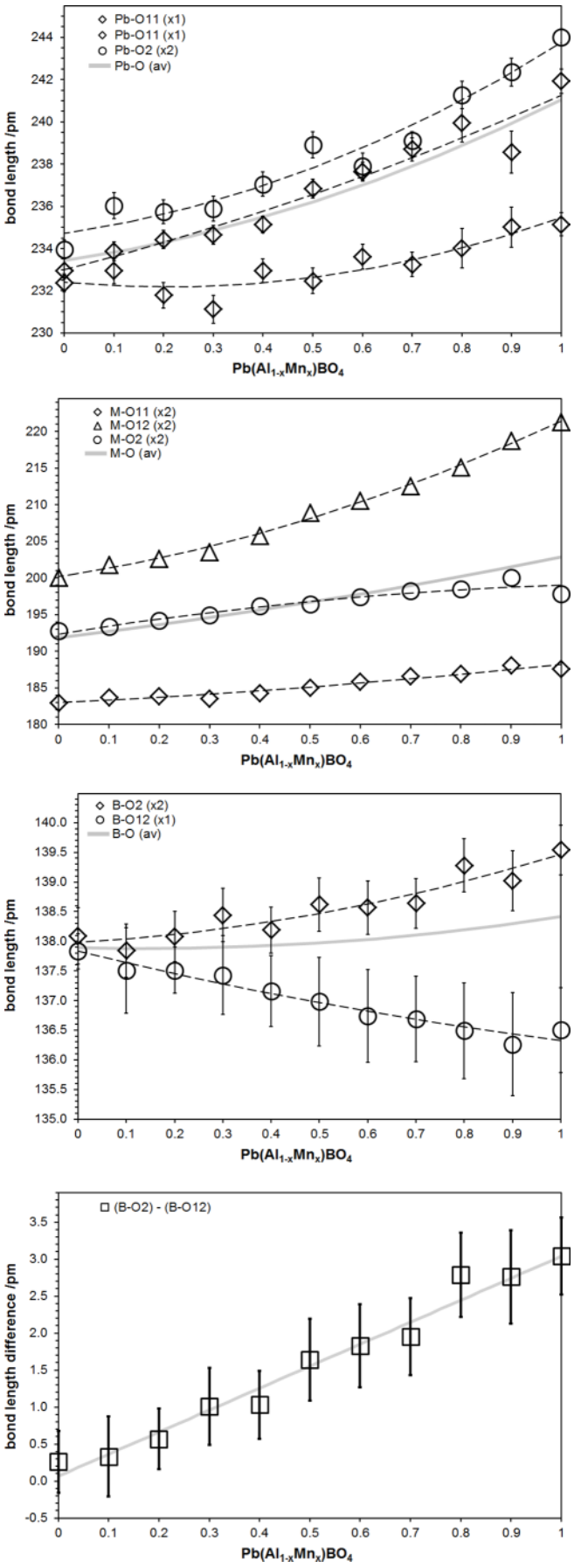

Fig. 6. Development of the interatomic distances and the bond length deviation of the BO_3-group in $Pb(Al_{1-x}Mn_x)BO_4$ with respect to the chemical composition calculated from the combined X-ray and neutron powder diffraction data refinement results.

either aluminum or manganese in the compounds for the phases having the respective higher contents. The Pb−O distances increase as well with increasing manganese content, which reflects the larger octahedral O11−O12 distances. It is interesting to note that for the aluminum compound the two different Pb−O11 distances with 232.4(4) pm and 234.0(3) pm are very close to each other, placing the lead atoms in the center between two different octahedra, whereas in the manganese end-member the respective distances are 235.2(5) pm and 241.9(6) pm. The two Pb−O2 distances are identical, because of the symmetry. If one takes into account that both lead and boron atoms interconnect the octahedral chains in an ordered manner these observations might be less surprising. With increasing manganese content the B−O12 distance decreases from 137.8(3) pm for $x = 0$ to 136.5(7) for $x = 1$ in the $PbAl_{1-x}Mn_xBO_4$ solid solution. In contrast the B−O2 distances increase from 138.1(5) pm to 139.5(4) pm (Fig. 6). This not only leads to an increase of the average B−O distances with increasing manganese content, but also to an increase of the bond difference between B−O2 and B−O12 bonds. Whereas this difference is nearly 0 for $PbAlBO_4$ (Fig. 6), which represents nearly D_{3h} symmetry, a deviation of 3.0(5) pm could be calculated for $PbMnBO_4$ representing the above mentioned C_S symmetry. Having the shortest and therefore strongest bond of the three different building units (BO_3, MO_6, PbO_4E) in this mullite-type compound, the BO_3 group is also influenced by the successive replacement of aluminum with manganese. This influence can be seen in the thermal behavior of the two end-members. Both phases show positive thermal expansion of the unit cell volume as well as for the *b* and *c* direction (Fig. 3). As can be seen from the thermal expansion coefficient (TEC) the expansion behavior is non-linear. Also for the *a* lattice parameters the TEC shows a non-linear behavior, but here the thermal expansion is negative for both end-members.

From the high-temperature neutron powder diffraction Rietveld refinements of $PbAlBO_4$ between 300 K and 870 K three different observations can be made. First, the BO_3 group, which is nearly symmetric at 300 K (B−O12 137.90(23) pm, B−O2 137.70(15) pm) has equivalent distances of 137.75(27) pm (B−O12) and 137.75(18) pm (B−O2) at 870 K; second, the AlO_6 octahedra as well as the PbO_4E polyhedra distort more with increasing temperature; third, the inclination angle ω [1] decreases from 78.40(3)° at 300 K to 77.99(3)° at 870 K. These observations clearly show that with increasing temperature the strong BO_3 bonds make this building unit symmetric, which distorts the other two cation polyhedra and leads to a tilt of the AlO_6 octahedra. This in turn elongates the *b*-direction at the expense of the *a*-direction. The tilting of the octahedra is limited to a small angle value and it is not completely clear if this is the only driving force for the negative thermal expansion of the *a* lattice parameter. Nevertheless, from the temperature-dependent lattice parameter change it is obvious that the negative expansion of the *a* lattice parameter and the positive expansion of the *b* lattice parameter are correlated. The same is the case for the $PbMnBO_4$ phase, but the negative thermal expansion of the *a* lattice parameter turns over to a slightly positive one at around

950 K. In the same temperature region the TEC of the *b*-direction becomes nearly 0 indicating also here an inflection of the thermal expansion. The internal energy for the thermal expansion of both end-members was calculated using the double-Debye-double-Einstein-Anharmonicity (DDEEA) volume equation of state for the single lattice parameters. It can be seen that the negative thermal expansion for $PbAlBO_4$ could best be described with two negative Einstein contributions for the negative thermal expansion whereas for $PbMnBO_4$ the Einstein k_{E2} parameter becomes positive. For the *b* lattice parameter this behavior is opposite, meaning k_{E2} is positive for $PbAlBO_4$ and negative for $PbMnBO_4$. Secondly the k_{D1} parameter for the low-temperature describable Debye contribution for $PbMnBO_4$ is negative, meaning that, from 0 K on, the thermal expansion of the *a* lattice parameter is negative. Nevertheless, one has to take into account that this contribution is small ($K_{D1} = -1.3(6) \cdot 10^{-12}$; Table 3) and could not be exactly determined unless highly accurate lattice parameters at very low temperatures are measured and evaluated. The same argument of non-accurate determination possibilities of the Debye contribution is true for the unit cell volume. On the other hand this contribution is an important factor to calculate the thermodynamic Grüneisen parameter as expression for the dependency of the phonon frequencies from the volume change (which is dependent from the temperature). From the DDEEA calculations of the volume behavior $k_{D1} = 8.2 \cdot 10^{-12}$ and $k_{D2} = 3.0 \cdot 10^{-12}$ are calculated for $PbAlBO_4$ which yields in an average $k_D = 5.6 \cdot 10^{-12}$ and $k_D = 2.9 \cdot 10^{-12}$ for $PbMnBO_4$. Since k_D could be expressed as equal to K_0/γ one can easily calculate the thermodynamic Grüneisen parameter if the bulk modulus K_0 is known.

Whereas for $PbAlBO_4$ we were able to determine the bulk modulus from pressure-dependent synchrotron X-ray powder data refinement results, these data are not available for $PbMnBO_4$. Therefore we carried out DFT calculations on the pressure-dependent volume change as well as the modification of global energy changes with changing unit-cell volume to theoretically calculate the bulk modulus using the 3rd-order Birch-Murnaghan isothermal equation of state in its pressure (Eq. (1a)) and energy (Eq. (1b)) form. It could be seen from Table 4 that the calculated values for the bulk modulus are very close to each other, which validates the results from the different theoretical approaches and moreover correlate well to the high-pressure diamond anvil cell experiments. The first derivative of the calculated bulk modulus is lower, but it is within the standard deviation when compared to the experimental value $K_0' = 8.3(13)$ for $PbAlBO_4$. Differences in K_0 and K_0' values could be attributed to different values of V_0 used and to the fact that K_0 and K_0' are inversely correlated. Based on results of theoretical calculations and experimentally obtained values of K_0 and K_0' for $PbAlBO_4$ it appears that the DFT calculations yield realistic values for the EoS parameters. Therefore it is fair to assume that the respective parameters calculated theoretically for $PbMnBO_4$ are also accurate.

Table 4. Experimental and theoretical Bulk moduli of $PbMBO_4$ (M = Al, Mn) evaluated by 3rd order B-M EoS.

Method	K_0/GPa	K_0'	V_0
$PbAlBO_4$			
Exp.	76.1(6)	8.3(13)	321.93(1)
DFT-E[a]	77.6(3)	6.9(21)	322.10(1)
DFT-P[a]	77.4(2)	6.5(19)	321.95(1)
$PbMnBO_4$			
Exp.	–	–	342.96(1)
DFT-E[a]	46.9(14)	8.4(23)	347.9(1)
DFT-P[a]	52.7(18)	8.4(36)	347.9(1)

a: P: pressure-dependent fit, E: energy-dependent fit

From the evaluated Debye fitting parameter k_{D1} and the calculated and experimental bulk moduli (76.1(6) GPa for $PbAlBO_4$ and 49.8(38) GPa for $PbMnBO_4$) it is possible to extract the thermodynamic Grüneisen parameter to be $\gamma_{Al} = 0.14(1)$ and $\gamma_{Mn} = 0.17(3)$ for $PbAlBO_4$ and $PbMnBO_4$, respectively. Surprisingly these values are rather small. Nevertheless, these are the first values published for mullite and mullite-type compounds known to have physical properties such as small thermal expansion or high creep resistance [1]. From the small change of internal energy with increasing temperature and the rigid behavior of the structural building units, mainly the BO_3 groups for these compounds; this could be a characteristic of this structural family. More detailed experiments are necessary to validate this hypothesis.

Conclusion

Upon manganese substitution in $PbAlBO_4$ the rigidity of BO_3 changes only slightly (including its planarity) leading to an insignificant degree of freedom for structural changes. Probably due to the highest distortion of the BO_3 group in $PbMnBO_4$ the thermal expansion coefficient of the *a* lattice parameter changes from negative to positive values at around 950 K.

The mullite-type $PbMBO_4$ seems to be intrinsically anharmonic at a very fundamental level associated with soft modes of PbO_4E, rigid modes of BO_3 and intermediate rigidity of MO_6. It is therefore reasonable to assume that neither the Einstein harmonic nor the Debye quasi-harmonic model adequately explain the thermal expansion of the materials, and adopting an anharmonic term is reasonable.

The characteristic Debye or Einstein temperature extracted from the thermal expansion simulations using a first order Grüneisen approach may significantly differ from that calculated using the second order Grüneisen approach; for simplicity and to reduce the number of refinable parameters we used the former one.

While M_0 and k_{D1} corresponds to the cell volume and γ/K_0 ratio (Grüneisen parameter/bulk modulus) at zero-pressure and 0 K, respectively, they refer only to corresponding hypothetical value for the cell parameter *a*, *b* and *c*.

Although V_0 is complementary between the experimental and the theoretical values, the uncertainly due to nonlinear extrapolation down to 0 K and the magneto-volume effect (restrict only to ferromagnetic $PbMnBO_4$ below

31 K [7]) cannot be ignored. The high characteristic temperatures might arise from this uncertainty. A careful binning of some oscillator frequencies in the distribution function can be tested during regression for corresponding realistic values but, of course, best would be to simulate using low-temperature data.

Acknowledgements. We gratefully acknowledge the Deutsche Forschungsgemeinschaft (DFG) for the financial support through the mullite-LEP project GE1981/4-1. TMG especially likes to thank the DFG for the support in the Heisenberg program (GE1981/3-1). The authors thank the Institut Laue-Langevin, Grenoble, France, for the allocation of neutron beam time. CBM, MC, and DH are grateful to CONICET and MINCYT. MC thanks specially CONICET for the doctoral scholarship. PEK, KEL and ALC acknowledge that portions of this work were performed at HPCAT (Sector 16), Advanced Photon Source (APS), Argonne National Laboratory. HPCAT operations are supported by DOE-NNSA under Award No. DE-NA0001974 and DOE-BES under Award No. DE-FG02-99ER45775, with partial instrumentation funding by NSF. APS is supported by DOE-BES, under Contract No. DE-AC02-06CH11357. Work at UNLV is supported by DOE award No. DEFG36-05GO08502. The UNLV High Pressure Science and Engineering Center is supported by the US Department of Energy, National Nuclear Security Administration, under Cooperative Agreement DE-FC08-01NV14049. A portion of this research at ORNL's Spallation Neutron Source, was sponsored by the Scientific User Facilities Division, Office of Basic Energy Sciences, U.S. Department of Energy and a portion of the high-pressure research is sponsored by FAME-Tech Labs fo the Department of Mechanical Engineering, UNLV.

References

[1] Fischer, R. X.; Schneider, H.: The mullite-type family of crystal structures. In *Mullite* (edited by H. Schneider and S. Komarneni), Wiley-VCH, Weinheim (2005) 1–46.
[2] Bystroem, A.; Westgren, A.: Arkiv foer Kemi, Mineral. Geol. **B16** (1943) 1–7.
[3] Garnier, P.; Calvarin, G.; Weigel, D.: J. Solid State Chem. **16** (1976) 55–62.
[4] Gavarri, J. R.; Weigel, D.; Hewat, A. W.: J. Solid State Chem. **23** (1978) 327–339.
[5] Park, H.; Barbier, J.: Acta Crystallogr. **E57** (2001) i82–i84.
[6] Park, H.; Barbier, J.; Hammond, R. P.: Solid State Sci. **5** (2003) 565–571.
[7] Park, H.; Lam, R.; Greendan, J. E.; Barbier, J.: Chem. Mater. **15** (2003) 1703–1712.
[8] Murshed, M. M.; Fischer, R. X.; Gesing, Th. M.: Z. Kristallogr. **227** (2012) 580–584.
[9] Murshed, M. M.; Gesing, Th. M.: Mater. Res. Bull. (2013) in press; http://dx.doi.org/10.1016/j.meterresbull.2013.05.007.
[10] Burianek, M.; Krenzel, Th. F.; Schmittner, M.; Schreuer, J.; Fischer, R. X.; Mühlberg, M.; Nénert, G.; Schneider, H.; Gesing, Th. M.: Int. J. Mater. Res. **103** (2012) 449–455.
[11] Murshed, M. M.; Nénert, G.; Gesing, Th. M.: Z. Kristallogr. NCS **227** (2012) 285–286.
[12] Gesing, Th. M.; Fischer, R. X.; Burianek, M.; Mühlberg, M.; Debnath, T.; Rüscher, C. H.; Ottinger, J.; Buhl, J. C.; Schneider, H.: J. Eur. Ceram. Soc. **31** (2011) 3055–3062.
[13] Murshed, M. M.; Rusen, A.; Fischer, R. X.; Gesing, Th. M.: Mater. Res. Bull. **47** (2012) 1323–1330.
[14] Pawley, G. S.: J. Appl. Crystallogr. **14** (1981) 357–361.
[15] Anderson, O. L.; Isaak, D. G.; Yamamoto, S.: J. Appl. Phys. **65** (1989) 1534–1543.
[16] Rivers, M.; Prakapenka, V. B.; Kubo, A.; Pullins, C.; Holl, C. M.; Jacobsen, S. D.: High Pressure Res. **28** (2008) 273–292.
[17] Murnaghan, F. D.: Proc. Nat. Acad. Sci. USA **30** (1944) 244–247.
[18] Birch, F.: Phys. Rev. **71** (1947) 809–824.
[19] Dovesi, R.; Orlando, R.; Civalleri, B.; Roetti, C.; Saunders, V. R.; Zicovich-Wilson, C. M.: Z. Kristallogr. **220** (2005) 571–573.
[20] Dovesi, R.; Saunders, V. R.; Roetti, C.; Orlando, R.; Zicovich-Wilson, C. M.; Pascale, F.; Civalleri, B.; Doll, K.; Harrison, N. M.; Bush, I. J.; D'Arco, P.; Llunell, M.: CRYSTAL09 (2009) CRYSTAL09 User's Manual. University of Torino, Torino.
[21] Bredow, T.; Gerson, A. R.: Phys. Rev. **B61** (2000) 5194–5201.
[22] http://www.crystal.unito.it/Basis_Sets
[23] Pascale, F.; Zicovich-Wilson, C. M.; Lopez, F.; Civalleri, B.; Orlando, R.; Dovesi, R.: J. Comput. Chem. **25** (2004) 888–897.
[24] Zicovich-Wilson, C. M.; Pascale, F.; Roetti, C.; Saunders, V. R.; Orlando, R.; Dovesi, R.: J. Comput. Chem. **25** (2004) 1873–1881.
[25] Senyshyn, A.; Boysen, H.; Niewa, R.; Banys, J.; Kinka, M.; Burak, Y.; Adamiv, V.; Izumi, F.; Chumak. I.; Fuess, H.: J. Phys. D: Appl. Phys. **45** (2012) 175305 (15 pp).
[26] Wallace, D. C.: Thermodynamics of Crystals, 1998 (Dover, New York).
[27] Shannon, R.: Acta Crystallogr. **A32** (1976) 751–767.
[28] Jahn, H. A.: Teller, E.: Proc. Royal. Soc. London, Ser. A Math. Phys. Sci. **161** (1937) 220–235.
[29] Wang, X.; Liebau, F.: Z. Kristallogr. **211** (1996) 437–439.